Ocean Engineering 235 (2021) 109043

Contents lists available at ScienceDirect

Ocean Engineering

journal homepage: www.elsevier.com/locate/oceaneng

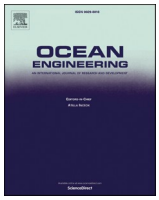

Simulation of vertical dispersion of oil droplets by Langmuir supercells through a Reynolds-averaged Eulerian formulation combined with Lagrangian particle tracking

A.J. Perez [a], F. Cui [b], J. Peñaloza-Gutierrez [c], S. Zeidi [a], N. Sinha [a], M. Boufadel [b], C. Smith [b], D. W. Murphy [c], A.E. Tejada-Martínez [a,*]

[a] Civil & Environmental Engineering, University of South Florida, Tampa, FL, USA
[b] Civil & Environmental Engineering, New Jersey Institute of Technology, Newark, NJ, USA
[c] Mechanical Engineering, University of South Florida, Tampa, FL, USA

ARTICLE INFO

Keywords:
Langmuir supercells
Vertical dispersion
Oil droplets
Discrete random walk model

ABSTRACT

Langmuir supercells (LS) are full-depth Langmuir circulations in unstratified shallow shelves. A Reynolds-averaged Eulerian formulation is developed resolving LS as a secondary component to the wind-driven mean shear current. This formulation is combined with Lagrangian particle tracking to investigate oil droplet entrainment induced by LS as a function of wind stress. Two cases are simulated, one in which 500-μm oil droplets are released into a steady field of LS generated by a wind stress of 0.1 N m^{-2} and waves of intermediate wavelength $\lambda = 6H$ where $H = 15$ m is the water column depth, significant amplitude of 0.6 m and period of 8 s. In the second case, the 500-μm oil droplets are released into a steady field of LS generated by the same wave forcing but with a weaker wind stress of 0.025 N m^{-2}. It is found that the greater wind stress leads to LS able to spread the droplets throughout upwelling and downwelling limbs of the cells within the first 80 minutes after release. The weaker wind leads to weaker LS that, within the same time after release, limit the dispersion of the droplets to the downwelling limbs of the cells forming Stommel retention zones for a prolonged time.

1. Introduction

Turbulence in the upper ocean is generated by a combination of surface winds, surface wave breaking, wave-current interaction and surface buoyancy. Wave-current interaction gives rise to Langmuir turbulence, characterized by a wide range of Langmuir circulation (LC) scales, parallel counter-rotating vortices roughly aligned in the direction of the wind. An LC vortex pair is sketched in Fig. 1. Wind speeds greater than approximately 3 m s^{-1} and winds roughly parallel to waves provide favorable conditions for the generation of Langmuir turbulence. The turbulence consists of small Langmuir scales emanating from the water surface which over time on the order of tens of minutes grow in depth and width typically reaching the base of the mixed layer in the upper ocean or the bottom of the water column in homogenous shallow water. This has been shown to be the case by Skyllingstad and Denbo (1995) for the upper ocean mixed layer.

It is well known that LC plays a major role towards the maintenance of the upper ocean mixed layer (Thorpe, 2004). In the case of the shallow coastal ocean 10–20 meters in depth, the field measurements of Gargett et al. (2004) and Gargett and Wells (2007) have shown that during the passage of storms when the water column becomes homogenous, LC can span the entire depth of the water column. Full-depth LC has been denoted as Langmuir supercells or LS due to their strong impact on the turbulence dynamics throughout the entire water column. Furthermore, the structure of coastal LS differs from the structure of ordinary LC in the upper ocean mixed layer, with LS being more coherent and intense (Shrestha et al., 2018). Gargett et al. (2004) and Gargett and Wells (2007) have shown that LS promote sediment re-suspension by sweeping sediments towards the bottom convergences of the vortices where the upwelling limbs of the cells can transport the particles upwards into the water column.

Surface oil slicks are commonly treated with dispersants to disintegrate the oil into droplets. Droplets may also form due to the persistent buffeting of surface breaking waves. The droplets can then be entrained and dispersed throughout the water column via the action of LC. As shown by Farmer and Li (1994), the downwelling limbs of the

* Corresponding author.
E-mail address: aetejada@usf.edu (A.E. Tejada-Martínez).

https://doi.org/10.1016/j.oceaneng.2021.109043
Received 28 September 2020; Received in revised form 21 March 2021; Accepted 18 April 2021
Available online 8 July 2021

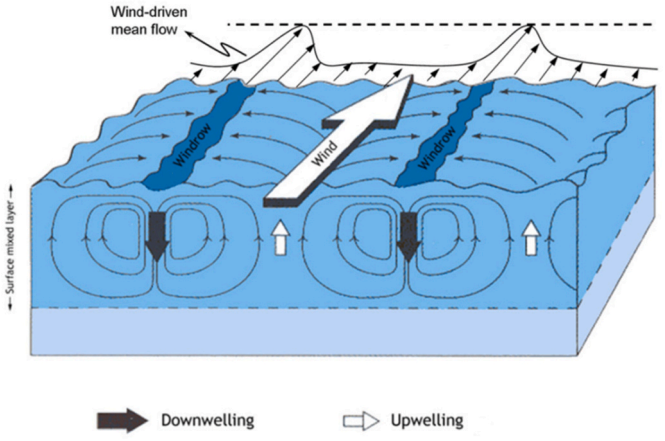

Fig. 1. Sketch of Langmuir cells.

counter-rotating vortices can exert vertical speeds greater than the buoyant rise speed of the droplets giving rise to submerged zones where the oil droplets can be retained for extended periods in what is referred to as Stommel retention zones (SRZs). Such retention zones were originally postulated by Stommel (1949). Thus, vertical dispersion of oil may be greatly enhanced during episodes of LC. Furthermore, in the case of an oil spill in coastal regions, given the observations of Gargett et al. (2004) and Gargett and Wells (2007), LS should serve as a mechanism for simultaneous entrainment of oil droplets and resuspension of sediments. Such instances could potentially lead to increased mixing between the sediments and oil and ultimately to the formation of oil-particle aggregates (OPAs) at offshore locations. OPAs are often thought to be formed near shore where sediments and oil come in direct contact.

Farmer and Li (1994) developed a model for oil droplet dispersion by LC. The model was based on an analytical representation of the largest LC scale with Lagrangian tracking of oil droplets via a random walk method. They found that over time the oil droplets can be homogenized about the SRZ due to the turbulence. The homogenization time depends on the inputted eddy viscosity associated with the Langmuir turbulence and physical characteristics of the oil droplets.

In this manuscript, an Eulerian Reynolds-averaged based methodology is introduced enabling a more accurate representation of LC than the analytical representation of Farmer and Li (1994), without the need to resort to more computationally intensive approaches such as large-eddy simulation (LES). The methodology is used to track oil droplets released at the water column surface in the presence of LS. The methodology relies on the coherency and persistence of LS. Here these cells are treated as a secondary component to the wind and/or pressure gradient-driven primary flow. As such, the Reynolds-averaged flow equations and the mesh are designed to resolve both the primary flow and the LS with the turbulence model accounting for the unresolved, smaller Langmuir scales.

In the new methodology, the flow equations consist of the Reynolds-averaged incompressible Navier-Stokes equations augmented with the Craik-Leibovich (C-L) vortex force parameterizing the wave-current interaction generating LC (Craik and Leibovich, 1976). The C-L vortex force allows for simulations to be performed with a flat surface, i.e. without resolution of the surface gravity waves that generate LC. Mathematically, the C-L vortex force consists of the cross product between the Stokes drift velocity induced by surface gravity waves and the resolved flow vorticity. The C-L vortex force is representative of the Stokes drift tilting of vertical vorticity associated with lateral shear towards the along-wind direction, resulting in LC.

Turbulence closure in the Reynolds-averaged formulation developed consists of the standard k-epsilon model updated to account for production of turbulent kinetic energy by Stokes drift shear and non-local transport induced by LS. The Reynolds-averaged methodology for computing the flow described above differs from previous methodologies dealing with Langmuir turbulence. Oftentimes Langmuir turbulence is computed via LES in which a majority of the Langmuir scales are resolved. A second approach more suitable to either general ocean circulation modeling or single water column modeling is based on Reynolds-averaging in which none of the Langmuir scales (including the largest LC scales) are resolved, and the turbulence model is left to account for the impact of the Langmuir turbulence on the resolved mean flow. The present methodology is based on Reynolds-averaging just as the previously described approach, however, the largest Langmuir scales, in this case the full-depth LS, are resolved.

In this manuscript, the new methodology will be used to investigate the vertical dispersion of oil droplets caused by LS. The new methodology computes the flow comprised of the mean flow plus the secondary LS structure, and the eddy viscosity and turbulent kinetic energy predicted by the k-epsilon model are used to perform Lagrangian tracking of oil droplets through a discrete random walk (DRW) method. The DRW approach of Gosman and Ioannides (1983) is adopted, in which the unresolved random fluctuations of the droplet trajectories are calculated by modeling the interaction between the droplets with randomly-generated eddies "that fit the statistics of the turbulence, velocity component root mean square and eddy lifetimes, as predicted by the turbulence model" (Javaherchi and Aliseda, 2016).

2. Reynolds-averaged flow equations and turbulence model

The Eulerian equations of fluid motion consist of the incompressible Reynolds-averaged continuity equation and the Reynolds-averaged Navier-Stokes (RANS) equation in (1) and (2), respectively, with the RANS equation augmented with the C-L vortex force parameterizing the generation of LC by the wave-current interaction:

$$\frac{\partial u_i}{\partial x_i} = 0 \tag{1}$$

$$\frac{\partial u_i}{\partial t} + u_j \frac{\partial u_i}{\partial x_j} = -\frac{1}{\rho}\frac{\partial \Pi}{\partial x_i} + \nu \frac{\partial^2 u_i}{\partial x_j^2} - \frac{\partial \overline{u_i' u_j'}}{\partial x_j} + \varepsilon_{ijk} U_j^S \omega_k \tag{2}$$

In this non-hydrostatic formulation, brackets denote Reynolds averaging; u_i is the i-th component of the Reynolds-averaged or mean velocity; ρ is the constant water density; Π is a modified mean pressure defined further below; ν is molecular kinematic viscosity; x_i is the coordinate in the i-th direction; t is time. The x_1, x_2 and x_3 directions are the downwind, crosswind and vertical directions, respectively. The last term on the right side of equation (2) is the C-L vortex force consisting of the cross product between the Stokes drift velocity vector U_i^S and the mean vorticity ω_i. The term ε_{ijk} in the C-L vortex force is the totally antisymmetric third rank tensor. Associated with the C-L vortex force is a modified pressure (McWilliams et al., 1997) defined in terms of the mean pressure p and Stokes drift as

$$\Pi = \frac{p}{\rho} + \frac{1}{2}\left[U_i^S U_i^S + 2u_i U_i^S\right] \tag{3}$$

In the present simulations, the Stokes drift velocity appearing in (2) and (3) will be taken to be purely aligned in the downwind direction and thus its components along the crosswind and vertical directions are zero. The downwind component follows the definition given by Phillips (1966):

$$U_2^S = U_3^S = 0$$

$$U_1^S = \sigma k a^2 \frac{\cosh(2kx_3)}{2\sinh^2(kH)} \tag{4}$$

where H is the water column depth and σ, k and a are the dominant frequency, wavenumber and amplitude, respectively, of the waves

generating LC. Note that $k = 2\pi/\lambda$ where λ is the dominant wavelength and k and σ may be related through the wave dispersion relation.

The Reynolds stress in (2) is modeled as

$$-u_i' u_j' = \nu_t \left(\frac{\partial u_i}{\partial x_j} + \frac{\partial u_j}{\partial x_i} \right) + \nu_t \left(\frac{\partial U_i^S}{\partial x_j} + \frac{\partial U_j^S}{\partial x_i} \right) \tag{5}$$

where the second term on the right side of (5) accounts for non-local transport induced by LC (Smyth et al., 2002; McWilliams et al., 2012; Harcourt, 2013; Sinha et al., 2014). In (5) the eddy viscosity is modeled based on the k-epsilon closure

$$\nu_t = C_\mu \frac{k^2}{\varepsilon} \tag{6}$$

where k and ε are the turbulent kinetic energy (TKE) and TKE dissipation rate, respectively. Note that this eddy viscosity is used for the momentum equation in all three directions. Following the standard k-epsilon model, the TKE and TKE dissipation rate are obtained by solving the following transport equations:

$$\frac{\partial k}{\partial t} + u_j \frac{\partial k}{\partial x_j} = \frac{\partial}{\partial x_j} \left[\left(\nu + \frac{\nu_t}{\sigma_k} \right) \frac{\partial k}{\partial x_j} \right] + G_k - \varepsilon \tag{7}$$

$$\frac{\partial \varepsilon}{\partial t} + u_j \frac{\partial \varepsilon}{\partial x_j} = \frac{\partial}{\partial x_j} \left[\left(\nu + \frac{\nu_t}{\sigma_\varepsilon} \right) \frac{\partial \varepsilon}{\partial x_j} \right] + C_{1\varepsilon} \frac{\varepsilon}{k} G_k + C_{2\varepsilon} \frac{\varepsilon^2}{k} \tag{8}$$

$$G_k = -u_i' u_j' \frac{\partial u_i}{\partial x_j} - u_i' u_j' \frac{dU_j^S}{dx_i} \tag{9}$$

where the TKE production, G_k, in (7) is taken as the traditional production by mean shear (first term on the right side of (9)) augmented by production by Stokes drift shear (second term on the right hand side of (9)) following Harcourt (2013). Note that the Reynolds stress in (9) is closed using the expression in (5). The values of the coefficients appearing in (6), (7) and (8) are $C_\mu = 0.09$, $\sigma_k = 1$, $\sigma_\varepsilon = 1.3$, $C_{1\varepsilon} = 1.44$ and $C_{1\varepsilon} = 1.92$ (Wilcox, 1994).

In the simulations to be presented below, the mean flow fields such as u_i contain the resolved mean wind-driven flow and the largest of the Langmuir cells while the fluctuating components such as u_i' contain the smaller unresolved scales.

3. Lagrangian particle tracking equations

The Lagrangian discrete phase model used to track oil droplets follows the Euler-Lagrange approach. The fluid phase is treated as a continuum by solving the Navier-Stokes equations as described earlier, while the dispersed phase is solved by tracking individual particles through the calculated flow field. In the Lagrangian discrete phase model, the trajectory of a discrete phase particle is predicted by integrating the force balance on each particle, which is written in a Lagrangian reference frame. This force balance equates the particle inertia with the forces (i.e., drag and buoyancy) acting on the particle, given as (Boufadel et al., 2018; Cui et al. 2018, 2020):

$$\frac{d\boldsymbol{u}_p}{dt} = \frac{3}{4} \frac{\rho}{\rho_p d_p} C_D \left(\boldsymbol{u} - \boldsymbol{u}_p \right) \left| \boldsymbol{u} - \boldsymbol{u}_p \right| - \widehat{\boldsymbol{k}}\, g \frac{(\rho_p - \rho)}{\rho_p} \tag{10}$$

where $\boldsymbol{u}$ is the fluid velocity, $\boldsymbol{u}_p$ is the oil droplet (particle) velocity, ρ_p is the particle density, ρ is the fluid density, d_p is the particle diameter, g is the gravity acceleration, and $\widehat{\boldsymbol{k}}$ is the unit vector in the vertical direction. The drag coefficient C_D in Eq. (10) is taken following Morsi and Alexander (1972) as

$$C_D = 0.4 + \frac{24}{Re_p} + \frac{6}{1 + \sqrt{Re_p}} \tag{11}$$

where Re_p is the relative Reynolds number defined as

$$Re_p = \frac{\rho_p d_p \left| \boldsymbol{u} - \boldsymbol{u}_p \right|}{\mu} \tag{12}$$

with μ the molecular dynamic viscosity of the fluid. Recall that the fluid phase velocity can be decomposed into mean velocity $\boldsymbol{u}$ and fluctuation velocity $\boldsymbol{u}'$ as

$$\boldsymbol{u} = \boldsymbol{u} + \boldsymbol{u}' \tag{13}$$

The mean velocity $\boldsymbol{u}$ can be obtained from solution of the RANS equations described earlier. The Cartesian components of the velocity fluctuation $\boldsymbol{u}' = (u_1', u_2', u_2')$ are defined through a DRW model (Gosman and Ioannides, 1983; Javaherchi and Aliseda, 2017) given as

$$u_i' = \xi_i \sqrt{2k/3} \tag{14}$$

where k is local turbulent kinetic energy and ξ_i is a random number following a zero-mean, unit-variance, normal distribution. The particle is assumed to interact with the fluid phase eddy over the smaller of the eddy lifetime and eddy crossing time. When this time is reached, a new value of the instantaneous velocity is obtained by applying a new value of ξ_i in Eq. (14). The eddy lifetime is defined as

$$T_L = 2C_L \frac{k}{\varepsilon} \tag{15}$$

where $C_L \sim 0.15$ is an empirical constant, and ε is the turbulent kinetic energy dissipation rate. The eddy cross time is defined as:

$$T_c = -\tau_p \ln \left[1 - \left(\frac{L_e}{\tau_p \left| \boldsymbol{u} - \boldsymbol{u}_p \right|} \right) \right] \tag{16}$$

where L_e is the eddy length scale, and can be estimated as

$$L_e = C_\mu^{3/4} \frac{k^{3/2}}{\varepsilon} \tag{17}$$

where the empirical constant $C_\mu \sim 0.9$ as before. The particle relaxation time τ_p is given by

$$\tau_p = \frac{\rho_p d_p^2}{18 \mu_w} \tag{18}$$

where d_p is the particle diameter. If $L_e > \tau_p \left| \boldsymbol{u} - \boldsymbol{u}_p \right|$, Eq. (16) does not have a solution, which indicates the droplet is captured by an eddy. Under this condition, the interaction time between turbulent eddy and droplet will be the eddy lifetime.

4. Computational setup

Simulations of LS tracking the motion of oil droplets induced by the

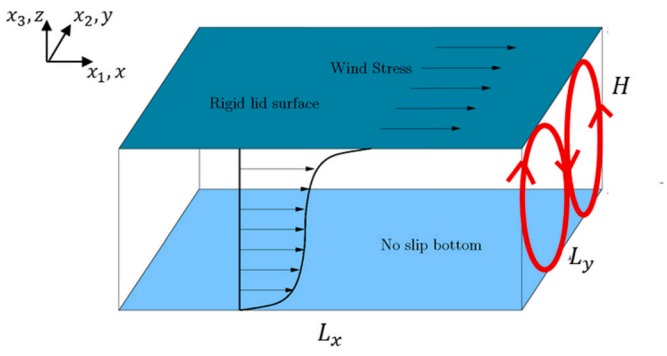

Fig. 2. Sketch of computational domain including the pattern of counter-rotating Langmuir cells to be resolved in the simulations.

cells will be performed for the problem configuration sketched in Fig. 2. The surface or top of the domain is a wind-sheared rigid lid leading to the primary flow with velocity arrows sketched in Fig. 2. The inclusion of the C-L vortex force in the momentum equation in (2) leads to the generation of LS with orientation sketched in Fig. 2. The bottom of the domain is taken as a flat, no-slip surface. Furthermore periodicity is taken along the downwind (x_1) and crosswind (x_2) directions.

Wind and wave forcing conditions are taken from the field measurements of Gargett et al. (2004) and Gargett and Wells (2007) during the presence of LS. In these measurements, the water column depth was $H = 15$ m. Furthermore, the wind stress was $\tau_{wind} = 0.1$ N m^{-2}, and the dominant amplitude, wavelength and period of the waves generating Langmuir cells were 0.6 m, $\lambda = 6H = 90$ m and 8 s, respectively. These conditions were also used to guide the large-eddy simulation (LES) of Tejada-Martínez and Grosch (2007).

Dimensionless parameters characterizing Langmuir cells are the wavelength-to-depth ratio λ/H and the turbulent Langmuir number. The latter is defined as $La_t = \sqrt{u_\tau/u_S}$ (McWilliams et al., 1997) where u_τ is the wind stress friction velocity given as $u_\tau = \sqrt{\tau_{wind}/\rho}$ and $u_S = \sigma k a^2$ where, as before, a is the dominant amplitude of the waves, k is the dominant wavenumber and σ is the dominant frequency. The turbulent Langmuir number is inversely proportional to wave forcing relative wind forcing. For the wind and wave forcing conditions described above, $\lambda/H = 6$ and $La_t = 0.7$.

Gargett and Grosch (2014) considered a turbulent Langmuir number based on bottom stress friction velocity in order to characterize the role of bottom stress on LS. Analyzing the data of Gargett et al. (2004) and Gargett and Wells (2007), they concluded that clear signatures of LS in their records were obtained when bottom friction velocity was approximately equal to surface (wind stress) friction velocity. Other instances of unstratified water columns were characterized by convection (driven by unstable surface buoyancy) or when the bottom friction velocity exceeded the wind stress friction velocity leading to shear-dominated turbulence near the bottom (caused by pressure gradient-driven flow, such as tidal flow) rather than Langmuir-dominated turbulence during LS events. Thus, the RANS simulations performed here as well as the LES of Tejada-Martínez and Grosch (2007) are characterized by the equilibrium condition of bottom stress matching the wind stress.

The domain is $L_x = 94.2$ m long in the downwind and $L_y = 62.8$ m wide in the crosswind following the LES of Tejada-Martínez and Grosch (2007). In particular, the value $L_y = 62.8$ m was chosen to resolve a pair of full-depth LS as expected from the field measurements of Gargett et al. (2004) (and as sketched in Fig. 2).

The Reynolds-averaged formulation will be tested with the domain discretized by a hexahedral mesh uniform in the downwind, crosswind and vertical directions. A mesh refinement study will be performed to demonstrate convergence of the solution. The resolution in the crosswind and vertical directions will be varied for three cases: coarse, fine, and refined uniform resolutions. The coarse mesh consists of 32 elements in the crosswind and 32 elements in the vertical, the fine mesh has 64 elements in the crosswind and vertical and the refined mesh has 128 elements in the crosswind and vertical. Based on the LES of Tejada-Martínez and Grosch (2007), in the mean when bottom stress matches the wind stress, full-depth Langmuir cells are steady and do not possess variation in the downwind direction (x_1), thus the Reynolds-averaged simulation will be taken as steady and two-dimensional and only 4 elements will be taken in the downwind direction for each mesh described above.

Given that the steady mean flow is 2-D and recalling the Stokes drift velocity in (4), the Reynolds-averaged continuity and momentum equations reduce to the following:

$$\frac{\partial u_2}{\partial x_2} + \frac{\partial u_3}{\partial x_3} = 0 \tag{19}$$

$$u_2\frac{\partial u_1}{\partial x_2} + u_3\frac{\partial u_1}{\partial x_3} = \nu\left(\frac{\partial^2 u_1}{\partial x_2^2} + \frac{\partial^2 u_1}{\partial x_3^2}\right) - \frac{\partial u_1' u_2'}{\partial x_2} - \frac{\partial u_1' u_3'}{\partial x_3} \tag{20}$$

$$u_2\frac{\partial u_2}{\partial x_2} + u_3\frac{\partial u_2}{\partial x_3} = -\frac{1}{\rho}\frac{\partial \Pi}{\partial x_2} + \nu\left(\frac{\partial^2 u_2}{\partial x_2^2} + \frac{\partial^2 u_2}{\partial x_3^2}\right) - \frac{\partial u_2' u_2'}{\partial x_2} - \frac{\partial u_2' u_3'}{\partial x_3} - U_1^S \omega_3 \tag{21}$$

$$u_2\frac{\partial u_3}{\partial x_2} + u_3\frac{\partial u_3}{\partial x_3} = -\frac{1}{\rho}\frac{\partial \Pi}{\partial x_3} + \nu\left(\frac{\partial^2 u_3}{\partial x_2^2} + \frac{\partial^2 u_3}{\partial x_3^2}\right) - \frac{\partial u_3' u_2'}{\partial x_2} - \frac{\partial u_3' u_3'}{\partial x_3} + U_1^S \omega_2 \tag{22}$$

The Reynolds-averaged continuity and momentum equations and the turbulence model described earlier are solved via a finite volume method ensuring pressure-velocity coupling through a staggered grid in which the pressure is computed at the cell faces (Patankar, 1980). A second order upwind scheme is used for the momentum, turbulent kinetic energy, and turbulent dissipation rate equations.

The solution will be compared with the LES of Tejada-Martínez and Grosch (2007) which was performed on a three-dimensional 32 x 64 x 96 mesh (i.e. 32 elements in the downwind, 64 elements in the crosswind and 96 elements in the vertical). The LES mesh was uniform over downwind and crosswind directions and stretched in the vertical to better resolve sharp vertical gradients near the surface and near the bottom. The interested reader is directed to Tejada-Martínez and Grosch (2007) for further details about the mesh and numerical discretization. Note that the LES is significantly more expensive than the Reynolds-averaged simulation. The LES takes about 1 week running on 16 parallel processors while the Reynolds-averaged solution takes about 20 minutes running on a single core desktop.

The previously described flow setup excludes the effect of Coriolis forcing from the momentum equations following the LES of Tejada--Martínez and Grosch (2007). The latter was guided by the field measurements of Langmuir supercells of Gargett and Wells (2007) characterized by the presence of tides and a geostrophic current in which the pressure gradient force was balanced by the Coriolis effect. Despite simplifications in the LES such as the exclusion of the geostrophic mean flow (Grosch and Gargett, 2016) and tidal flow that were measured in the field, the LES-resolved Langmuir supercells were coherent throughout the entire depth of the water column in agreement with the field measurements (Tejada-Martínez and Grosch, 2007; Gargett and Wells, 2007; Tejada-Martínez et al., 2009). The full-depth coherency of the cells in both the field measurements and the LES was attributed to the active Stokes drift shear near the bottom induced by the intermediate waves generating the cells and to the weak crosswind components of the tidal and geostrophic flows relative to the downwind current in the field and the complete absence of the tidal and geostrophic flows in the LES.

Following Tejada-Martínez and Grosch (2009), subsequent shallow-water LES of Langmuir supercells (Kukulka et al., 2011; Martinat et al., 2011; Akan et al., 2013; Shrestha et al., 2018, 2019; Shrestha and Anderson, 2020) have excluded the Coriolis effect. In contrast, LES of Langmuir cells in the upper ocean mixed layer over deep water normally include rotational terms which produce an oscillating inertial current that rotates off the wind/wave direction with time (i.e. the Ekman spiral), breaking up originally coherent Langmuir cells into much less organized structures (McWilliams et al., 1997). In this case, the turbulence may be considered "steady'' (i.e. under statistical equilibrium) only when averaged over periods of the inertial current as discussed by Tejada-Martínez et al. (2009). Grosch and Gargett (2016) demonstrated analytically how the results of the shallow water LES of Langmuir supercells without the Coriolis effect are nonetheless valid in comparison to the field measurements of Langmuir supercells made under the effect of rotation in the presence of a coastal boundary. Specifically, Grosch and Gargett (2016) showed the first-order equivalency between two steady mean flows (case A and case B) resulting from the action of a constant wind stress on a shallow unstratified water column. Case A is obtained with rotation and a lateral boundary to the right of

the direction of the wind stress (similar to the Gargett et al. field measurements of LS) and case B is obtained without rotation and without a lateral boundary. The various shallow water LES of Langmuir supercells referenced above and the analogous RANS simulations presented here follow case B.

5. Reynolds-averaged vs. LES resolved flow comparison

The Reynolds-averaged solution is first compared with LES in terms of steady state velocity fluctuations characterizing the resolved full-depth Langmuir cells or LS. In LES, the velocity fluctuations associated with LS are obtained as described by Tejada-Martínez and Grosch (2007). First, the LES-resolved velocity is decomposed following the classical Reynolds decomposition:

$$u_i^{LES} = u_i^{LES}x, y, t + u_i^{LES'} \tag{23}$$

where $u_i^{LES}x, y, t$ is the mean component obtained by averaging the statistically steady u_i^{LES} velocity field over the downwind and crosswind directions and over time. The LES-resolved velocity fluctuations, $u_i^{LES'}$, are decomposed into a component induced by LS, v_i^{LES}, and a component induced by scales smaller than LS, $u_i^{LES''}$:

$$u_i^{LES'} = v_i^{LES} + u_i^{LES''} \tag{24}$$

where

$$v_i^{LES} = u_i^{LES'}{}_{x,t} \tag{25}$$

Note that $u_i^{LES'}$ denotes the LES-resolved fluctuations which include the LS-induced fluctuations plus fluctuations induced by scales smaller than LS. LS is persistent over time and coherent in the downwind direction, thus fluctuations associated with LS can be extracted by averaging $u_i^{LES'}$ over time and over the downwind direction as expressed in (25).

The steady LS-induced fluctuation in the Reynolds-averaged formulation in (19)-(22) can be obtained as follows. First, re-express the Reynolds-averaged solution from (19)-(22) as

$$u_i^{RANS} = u_i \tag{26}$$

The Reynolds-averaged solution (i.e. the RANS solution) can then be decomposed as

$$u_i^{RANS} = u_{ix,y} + v_i^{RANS} \tag{27}$$

where the primary component $u_{ix,y}$ is the steady state RANS solution averaged over the streamwise and spanwise directions and the secondary v_i^{RANS} is the LS-induced fluctuation. Thus, in post-processing, the latter may be obtained from (27) as simply

$$v_i^{RANS} = u_i^{RANS} - u_{ix,y} \tag{28}$$

Fig. 3 shows the structure of the resolved LS through LES and RANS solutions in terms of v_i^{LES} and v_i^{RANS}, respectively, over the crosswind/vertical extent of the computational domain. Panels (a)-(c) correspond to LES and (d)-(f) correspond to the RANS solution. The RANS solution shown was obtained with the fine mesh 4 x 64 x 64 resolution described earlier. Panels (a) and (c) show the full-depth downwelling and upwelling limbs of the LS resolved by the LES and RANS solutions, respectively, in terms of vertical velocity fluctuations. The downwelling limb is revealed by a full-depth region of negative vertical velocity fluctuation and the upwelling limb is revealed by a full-depth region of positive velocity fluctuation.

Notice that the top of the downwelling limb corresponds to the surface convergence of the LS seen on panels (b) and (d) in terms of the crosswind velocity fluctuation. Also notice that both LES and RANS downwind velocity fluctuations in panels (c) and (f), respectively, are characterized by a full-depth region of positive values coinciding with the downwelling limbs of the cells (panels (a) and (d)). Furthermore, these full-depth regions of positive downwind velocity fluctuations are intensified near the bottom. This near-bottom intensification of downwind velocity fluctuations is a key signature of LS that distinguishes it from LC in the upper ocean mixed layer (Gargett et al., 2004; Gargett and Wells, 2007).

The cell pattern and velocity fluctuation magnitudes obtained with the LES in panels (a)–(c) of Fig. 3 is in good agreement with the full-depth LC measurements of Gargett and collaborators. This good agreement has been highlighted by Tejada-Martínez et al. (2009). Furthermore, it is seen in Figure (3) that the Reynold-averaged formulation is able to capture the overall structure of LS (panels (d)-(f)) consistent with the LES.

The behavior of the turbulence model can be seen in Fig. 4 in terms of predicted eddy lifetimes and eddy length scales. Note that eddy length scales and lifetimes are important for the prediction of turbulent dispersion of the oil droplets through equations (10)-(18). As expected, the smallest length scales occur near the surface and near the bottom and in the bulk of the water column the eddy length scale reaches approximately 12 m, comparable to the water column depth of 15 m. Additionally, the shorter eddy lifetimes correspond to the smallest eddies near the surface and bottom and the longer eddy lifetimes correspond to the larger eddies spanning the depth of the water column.

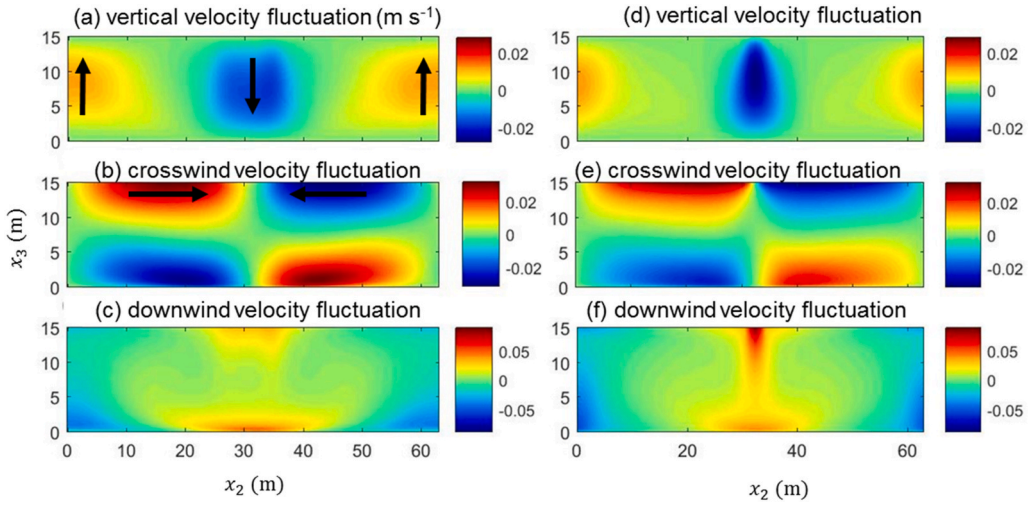

Fig. 3. Velocity fluctuations induced by LS, v_i, resolved in LES (a)–(c) and in the new RANS formulation (d)–(f), shown over the crosswind-vertical (x_2–x_3) plane. The downward and upward arrows in panel (a) denote the full-depth dowelling and upwelling limbs of the cell resolved in the LES in terms of vertical velocity fluctuations. Similar upwelling and downwelling limbs are resolved by the RANS solution (panel (d)). The right and left arrows denote in panel (b) denotes the surface convergence of the cell resolved in LES. A similar surface convergence zone is resolved by the RANS solution.

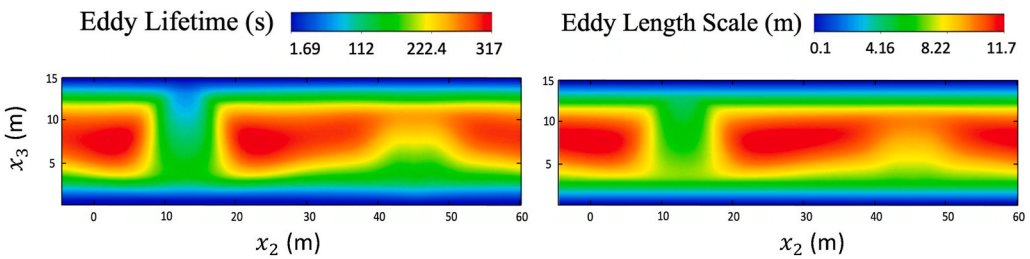

Fig. 4. Eddy lifetime (T_L) and eddy length scale (L_e) in a statistically steady state LS field generated by wind and wave forcing characterized by $La_t = 0.7$ and $\lambda / H = 6$.

Figs. 5 and 6 present depth-profiles of the velocity variances and mean downwind velocity characterizing LS, respectively, obtained with the Reynolds-averaged formulation with the three levels of mesh resolution described earlier (coarse, fine and refined meshes). These figures show that the mesh refinement leads to convergence of the solution as no significant differences are observed between the fine and refined mesh solutions. The mesh refinement study also suggests that the Reynolds-averaged formulation could be improved (for example through calibration of the turbulence model coefficients in equations (6)–(9)) in order to obtain better agreement with the LES. Nevertheless, the Reynolds-averaged solution is consistent with the LES solution in terms of the LS structure, as seen in Fig. 3 described earlier. Furthermore, it can be seen that the downwind velocity variance (panel (a) in Fig. 5) is characterized by near-bottom intensification in both the Reynolds-averaged and LES solutions. This is associated with the near-bottom intensification of downwind velocity fluctuations, a key signature of LS as described earlier. Furthermore, the crosswind velocity fluctuations are intensified near the surface relative to the middle of the water column (panel (b) in Fig. 5). This intensification is induced by the surface convergences of the LS, described earlier. Finally, Fig. 6 shows that the level of vertical homogenization of mean downwind velocity induced by LS is nearly the same for all Reynolds-averaged solutions in good agreement with the LES. This is reflected through the near flat velocity profiles throughout the bulk of the water column.

Given that no significant differences are observed between the fine and refined mesh Reynolds-averaged solutions, results from the fine mesh solution will be presented for the remainder of this manuscript.

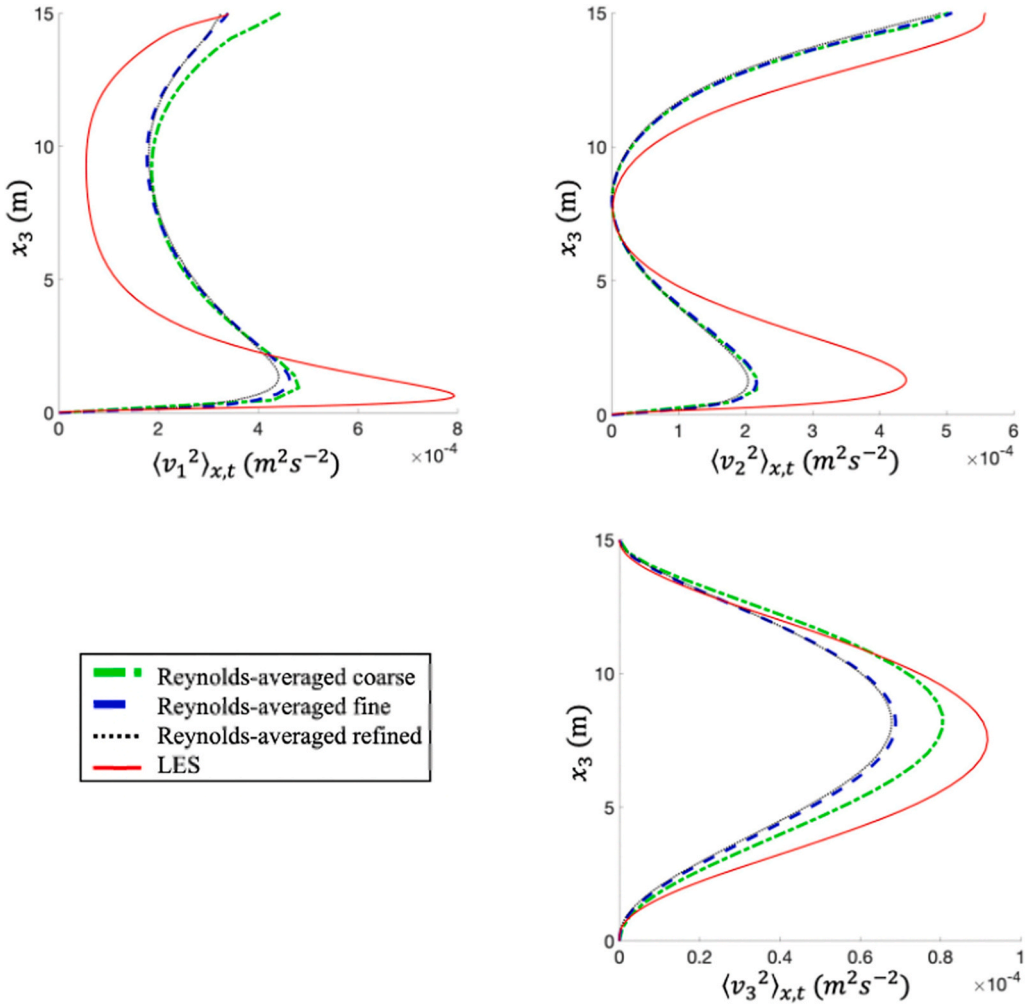

Fig. 5. Velocity variance induced by LS resolved in LES and in the new RANS formulation.

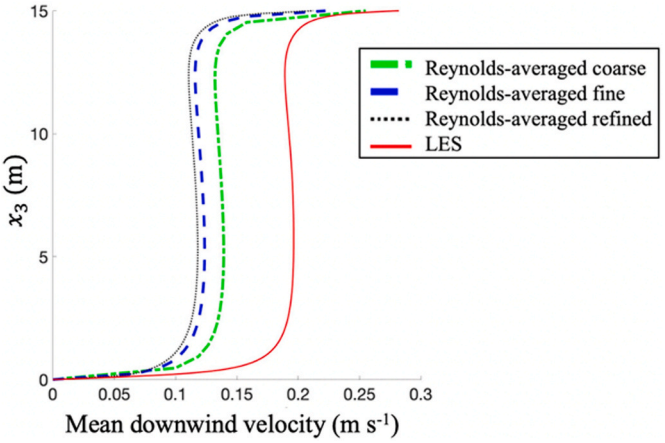

Fig. 6. Mean velocity, $u_{1x,y,t}$ resolved in the new RANS formulation.

6. Oil dispersion via Lagrangian particle tracking

To explore the impact of LS on dispersion of oil droplets, two simulations were conducted tracking the oil droplets under different wind stress. In the first simulation, the wind and wave forcing conditions are the same as in the LS simulation presented in the previous section. Recall that in this simulation the water column depth was $H = 15$ m. Furthermore, the wind stress was $\tau_{wind} = 0.1$ N m^{-2}, and the dominant amplitude, wavelength and period of the waves generating Langmuir cells were $a = 0.6$ m, $\lambda = 90$ m and $T = 8$ s, respectively. For these parameters, the dimensionless wind and wave forcing parameters are $La_t = 0.7$ and $\lambda/H = 6$ (i.e. $\lambda = 90$ m). The second LS simulation is characterized by a lower wind stress $\tau_{wind} = 0.025$ N m^{-2} and with the same wave characteristics as the first simulation. Thus $La_t = 0.5$ and $\lambda/H = 6$. Such a change in parameters from simulation 1 to simulation 2 corresponds to a scenario in which the winds calm down while the waves (amplitude and wavelength) remain constant. This was observed in the field by Gargett et al. (2004) during their measurements of LS (Ann Gargett, personal communication) as the waves did not respond immediately to a change in wind. Other researchers have adopted a similar approach, for example, in their LES, Li and Song (2012) kept the wave field fixed while changing wind speed to investigate the effect of wind speed on the spacing between Langmuir cells. This type of scenario can come about if the waves are non-locally generated such as swell waves.

Fig. 7 shows the vertical and crosswind velocity fluctuations and turbulent kinetic energy (TKE) induced by LS generated with wind stress $\tau_{wind} = 0.1$ N m^{-2} and $\tau_{wind} = 0.025$ N m^{-2}, respectively. Stronger wind leads to more intense cells in terms of downwelling and upwelling vertical velocity fluctuations and in terms of surface cell convergence and bottom cell convergence (represented through crosswind velocity fluctuations). In both cases, elevated values of TKE are caused by the convergence of the cells at the surface and by the downwelling limbs of the cells impinging at the bottom, with the $\tau_{wind} = 0.1$ N m^{-2} case providing the greatest TKE values.

As seen in Fig. 8 in the case with $\tau_{wind} = 0.025$ N m^{-2}, throughout the duration of the simulation (4800 seconds or 80 minutes), the majority of the 500-μm oil droplets released at the surface remain within the downwelling limb of the cell forming the so-called Stommel retention zone (SRZ). The upwelling limb of the cell is not active in driving vertical transport, but some of the droplets do rise back to the surface primarily due to buoyancy. In the case with $\tau_{wind} = 0.1$ N m^{-2} in Fig. 9, the droplets initially accumulate within the downwelling limb of the cell and are forced to the bottom of the water column much more rapidly

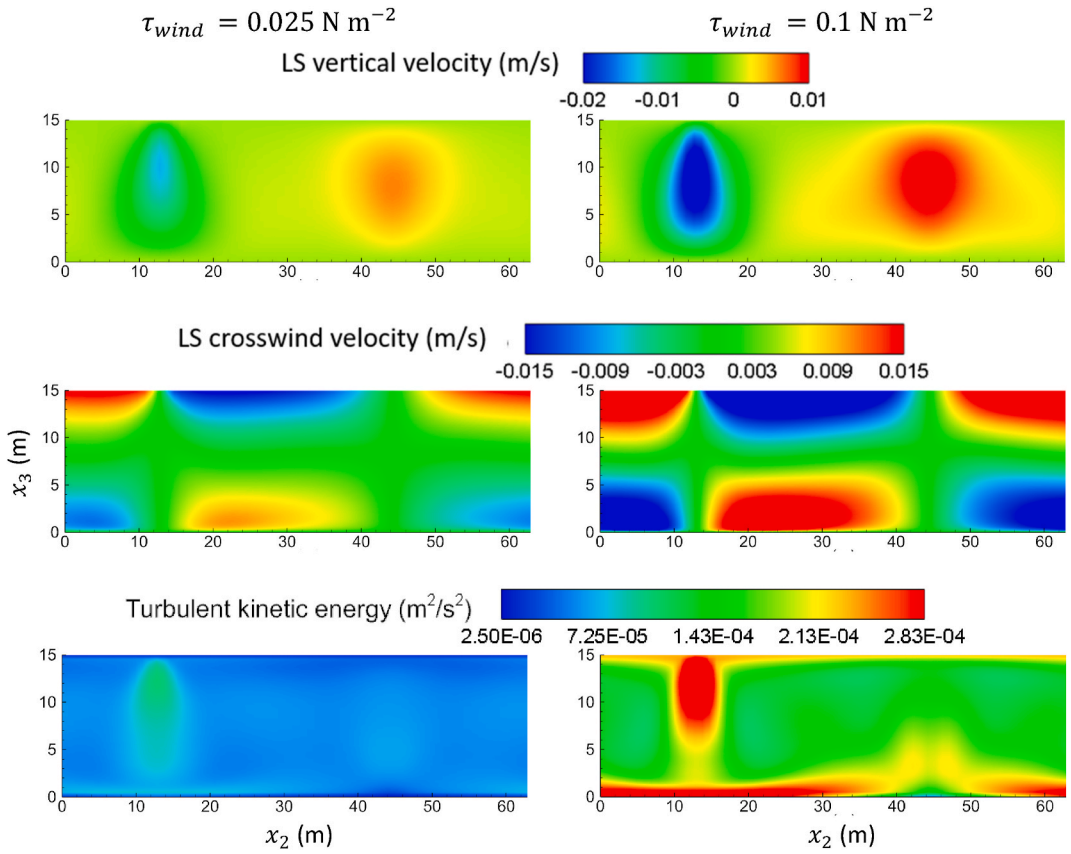

Fig. 7. Resolved LS velocity fluctuations and turbulent kinetic energy (TKE) obtained from the k-epsilon closure for wind and wave forced flows. One pair of LS is resolved.

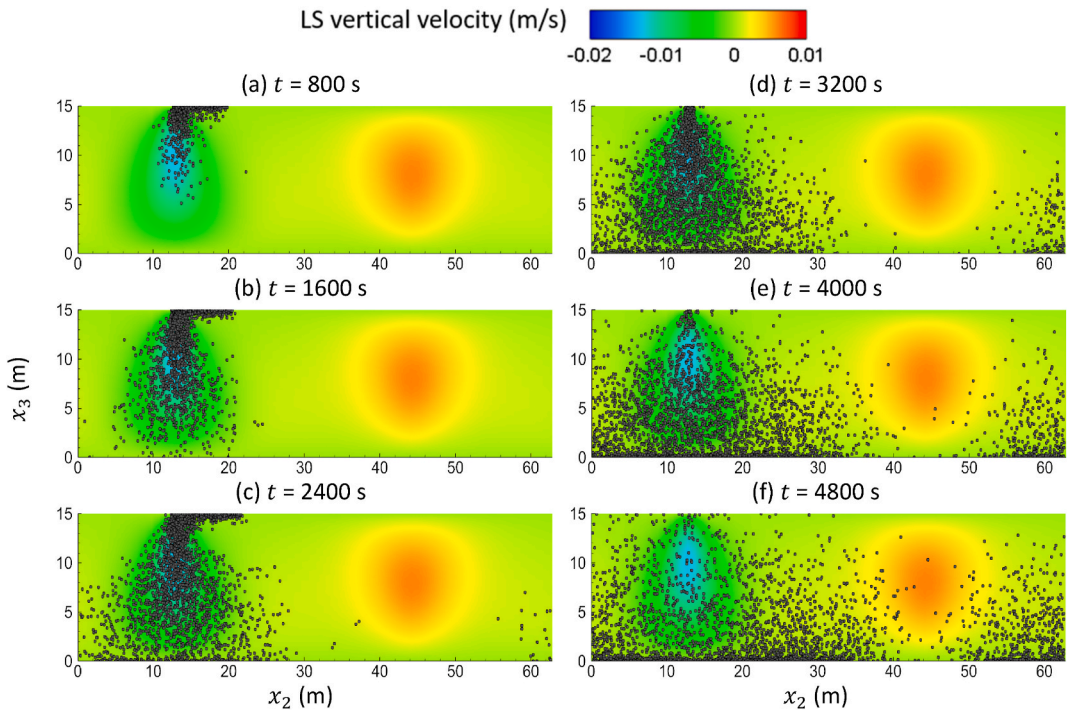

Fig. 8. Snapshots of 500-μm oil droplets after oil droplets released from the surface above a steady state LS field generated by wind and wave forcing characterized by, $\tau_{wind} = 0.025$ N m^{-2}, $La_t = 0.5$ and $\lambda/H = 6$. Oil density is 887 kg m^{-3}. Water density is taken as 1000 kg m^{-3}. Color contours show downwelling and upwelling limbs of LS. Note that the formation of the Stommel retention zone at the downwelling. (For interpretation of the references to colour in this figure legend, the reader is referred to the Web version of this article.)

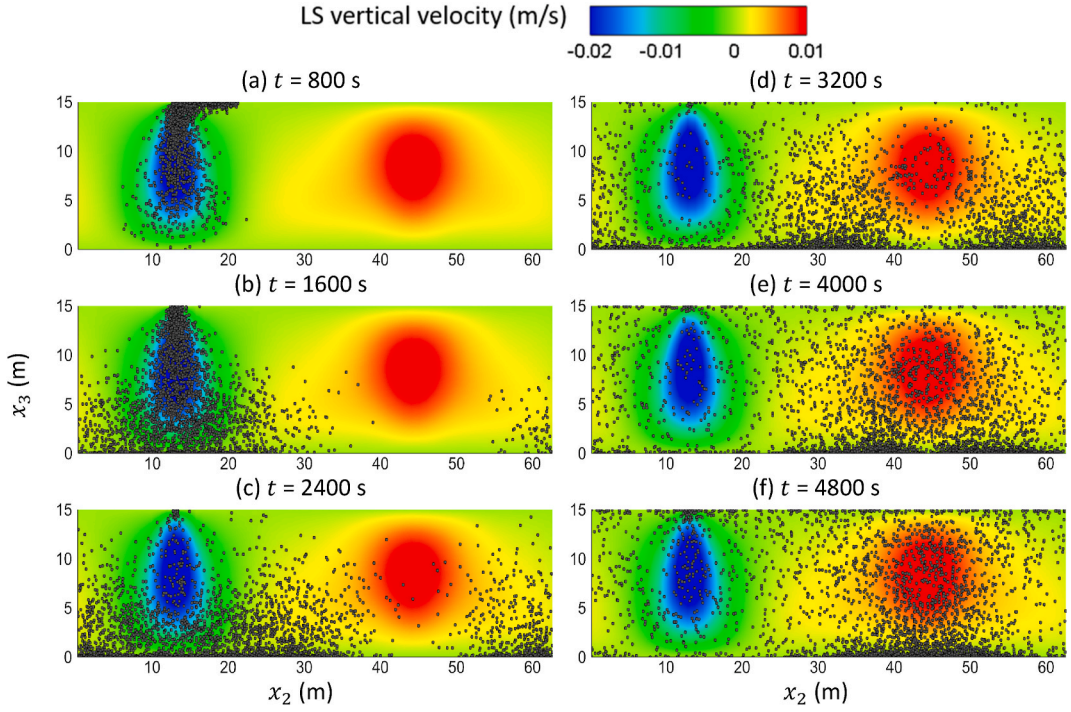

Fig. 9. Snapshots of 500-μm oil droplets after oil droplets released from the surface in a statistically steady state LS field generated by wind and wave forcing characterized by, $\tau_{wind} = 0.1$ N m^{-2}, $La_t = 0.5$ and $\lambda/H = 6$. Oil density is 887 kg m^{-3}. Water density is taken as 1000 kg m^{-3}. Color contours show downwelling and upwelling limbs of LS. (For interpretation of the references to colour in this figure legend, the reader is referred to the Web version of this article.)

than the case with $\tau_{wind} = 0.05$ N m^{-2}. In the stronger wind case (Fig. 9), droplets begin reaching the bottom of the water column by about 800 seconds (13.3 minutes) of the simulation, whereas in the weaker wind case (Fig. 8), at this time the droplets are still approximately 5 meters above the bottom. In the case of $\tau_{wind} = 0.1$ N m^{-2}, by 4800 seconds or 80 minutes, the majority of the droplets have been swept underneath the upwelling limb of the cell to be advected back to the surface by the positive vertical velocity in this region of the cell (Fig. 9). In both

simulations the droplet distribution becomes more homogenous over time and the results with $\tau_{wind} = 0.1$ N m^{-2} indicate a homogenization about both the upwelling and downwelling limbs of LS. In the case of Langmuir circulation in the upper ocean mixed layer, where the downwelling limbs of the cells are narrower and more intense than the upwelling limbs, homogenization of droplets typically occurs only about the downwelling limbs (i.e. the SRZs) (Farmer and Li, 1994).

To ensure accuracy, the time step of the Lagrangian particle tracking ($\Delta t = 2.2 \times 10^{-5}$ s) is taken smaller than the particle relaxation time (τ_p given in Eqn. (18)) and the eddy lifetime ($T_L = 2C_L\, k/\varepsilon$) given earlier in Eqn. (15)). Furthermore, recall that the particle is assumed to interact with the fluid phase eddy over the smaller of the eddy lifetime (Eqn. (15)) and eddy crossing time (Eqn. (18)). When this time is reached, a new value of the instantaneous/fluctuating velocity is obtained by applying a new value of the random number ξ_i in Eqn. (14). For example, in the simulation with $\tau_{wind} = 0.1$ N m^{-2} within the downwelling limb of the cell, the eddy length scale is $L_e > \tau_p|\boldsymbol{u} - \boldsymbol{u}_p|$ since $L_e \sim 5$ m (see Fig. 4), $|\boldsymbol{u}_p| \sim |\boldsymbol{u}|$ and $\tau_p = 6.5 \times 10^{-5}$ s. As such, the expression for eddy cross time (Eqn. (16)) is not defined. Under this condition, the interaction time between turbulent eddy and droplet will be the eddy lifetime $T_L \sim 160$ s (see Fig. 4) and thus a new value of ξ_i is applied at every 160 s. Thus, excessive droplet dispersion would occur within the downwelling limb of the cell if instead a new value of ξ_i were to be applied, say, at every time step ($\Delta t = 2.2 \times 10^{-5}$ s).

7. Conclusions

A Reynolds-averaged methodology capturing full-depth Langmuir supercells or LS in shallow water was presented showing consistent agreement with LES. In the presence of oil broken up into droplets at the surface of the sea, LS serve to entrain the droplets along the downwelling limbs of the cells. Lagrangian particle tracking simulations demonstrated the entrainment and overall distributions of 500-μm oil droplets induced by LS as function of time and LS intensity in a water column 15 m in depth. A 0.1 N m^{-2} wind stress and intermediate waves with significant wavelength, amplitude and period of 90 m, 0.6 m and 8 s respectively, led to LS capable of transporting the oil droplets throughout both downwelling and upwelling limbs of the cells within 80 minutes of droplet release. Over time, the droplet distribution homogenized about both limbs of the cells. Meanwhile, a lower wind stress of 0.025 N m^{-2} with the same wave field previously described led to weaker LS structure accumulating the droplets within its downwelling limb, and thus forming SRZs, over a prolonged time extending throughout at least the first 80 minutes after droplet release.

In addition to providing a less computationally expensive alternative to LES, the Reynolds-averaged methodology for capturing the largest scales of Langmuir circulation introduced and its coupling with either Lagrangian particle tracking or population balance equations would be suitable to predict processes such as oil weathering, sediment flocculation and the formation of oil-particle aggregates. The latter two processes should be promoted at the surface convergence zones of the cells and underneath the downwelling limbs of the cells, where the greatest values of TKE were observed. These areas of research will be explored in the future. Furthermore, this methodology should permit future investigations of the interaction between Langmuir cells and other processes such as river plumes and rip currents in the coastal ocean nearshore regions for which LES may prove cost prohibitive. Coupling with either Lagrangian particle tracking or scalar transport should allow for the investigation of the resulting vertical and lateral transport induced by Langmuir cells in these complex and realistic settings.

In order to realize its potential, the newly introduced methodology needs to be improved through calibration of turbulence model coefficients. The values of the turbulence model coefficients appearing in Eqns. (6), (7) and (8) were taken simply as default values and in the future should be re-calibrated to represent Langmuir turbulence. Furthermore, the DRW model coefficient in Eqn. (15) was taken as a default value of $C_L = 0.15$. However, as noted by Javaherchi and Aliseda (2016), calibration of this coefficient through experimental data from various applications has led to a range between 0.0675 and 0.205. Furthermore, as they point out, inaccurate values of this timescale constant can lead to gross under- or overestimation of the particle dispersion process.

CRediT authorship contribution statement

A.J. Perez: Software, Validation, Visualization. **F. Cui:** Software, Validation, Visualization. **J. Peñaloza-Gutierrez:** Software, Validation, Visualization. **S. Zeidi:** Software. **N. Sinha:** Software. **M. Boufadel:** Conceptualization, Methodology, Supervision. **C. Smith:** Conceptualization, Methodology. **D.W. Murphy:** Conceptualization, Methodology. **A.E. Tejada-Martínez:** Conceptualization, Methodology, Supervision, Writing, Project administration, Funding acquisition.

Declaration of competing interest

The authors declare that they have no known competing financial interests or personal relationships that could have appeared to influence the work reported in this paper.

Acknowledgement

This research was made possible by a grant from the Gulf of Mexico Research Initiative. Data are publicly available through the Gulf of Mexico Research Initiative Information & Data Cooperative (GRIIDC) at https://data.gulfresearchinitiative.org (doi: 10.7266/JXE8ZBNV).

References

Akan, C., Tejada-Martínez, A.E., Grosch, C.E., Martinat, G., 2012. Scalar transport in large-eddy simulation of Langmuir turbulence in shallow water. Continent. Shelf Res. 55.
Boufadel, M.C., Cui, F., Katz, J., Nedwed, T., Lee, K., 2018. On the transport and modeling of dispersed oil under ice. Mar. Pollut. Bull. 135, 569–580.
Craik, A.D., Leibovich, S., 1976. A rational model for Langmuir circulations. J. Fluid Mech. 73 (3), 401–426.
Cui, F., Boufadel, M.C., Geng, X., Gao, F., Zhao, L., King, T., Lee, K., 2018. Oil droplets transport under a deep-water plunging breaker: impact of droplet inertia. J. Geophys. Res.: Oceans 123 (12), 9082–9100.
Cui, F., Zhao, L., Daskiran, C., King, T., Lee, K., Katz, J., 2020. Modeling oil dispersion under brekaing waves. Part II: coupling Lagrangian particle tracking with population balance model. Environ. Fluid Mech.
Farmer, D., Li, M., 1994. Oil dispersion by turbulence and coherent circulations. Ocean Eng. 21, 575–587.
Gargett, A.E., Wells, J.R., Tejada-Martínez, A.E., Grosch, C.E., 2004. Langmuir supercells: a mechanism for sediment resuspension and transport in shallow seas. Science 306, 1925–1928.
Gargett, A.E., Wells, J.R., 2007. Langmuir turbulence in shallow water. Part I. Observations. J. Fluid Mech. 576, 27–61.
Gargett, A.E., Grosch, C.E., 2014. Turbulence process domination under the combined forcings of wind stress, the Langmuir vortex force, and surface cooling. J. Phys. Oceanogr. 44, 44–67.
Gosman, A.D., Ioannides, E., 1983. Aspects of computer simulation of liquid-fueled combustors. J. Energy 7 (6), 482–490.
Grosch, C.E., Gargett, A., 2016. Why do LES of Langmuir supercells not include rotation? J. Phys. Oceanogr. 46.
Harcourt, R.R., 2013. A second-moment closure model of Langmuir turbulence. J. Phys. Oceanogr. 43, 673–697.
Javaherchi, T., Aliseda, A., 2016. The transport of suspended sediment in the wake of a marine hydrokinetic turbine: simulations via a validated Discrete Random Walk (DRW) model. Ocean Eng. 129, 529–537.
Kukulka, T., Plueddemann, A., Trowbridge, J., Sullivan, P., 2011. The influence of crosswind tidal currents on Langmuir circulation in a shallow ocean. J. Geophys. Res. 116.
Li, Shuang, Song, J., 2012. The spacing of Langmuir circulation under modest wind. Chin. J. Oceanol. Limnol. 30, 690–696.
Martinat, G., Xu, Y., Grosch, C.E., Tejada-Martínez, A.E., 2011. LES of turbulent surface shear stress and pressure-gradient-driven flow on shallow continental shelves. Ocean Dynam. 61.
McWilliams, J.C., Sullivan, P.P., Moeng, C.-H., 1997. Langmuir turbulence in the ocean. J. Fluid Mech. 334, 1–30.

McWilliams, J.C., Huckle, E., Liang, J., Sullivan, P., 2012. The wavy Ekman layer: Langmuir circulations, breakers, and Reynolds stress. J. Phys. Oceanogr. 42, 1793–1816.
Morsi, A.J., Alexander, S.A., 1972. An investigation of particle trajectories in two-phase flow system. J. Fluid Mech. 55, 193–208.
Patankar, S.V., 1980. Numerical Heat Transfer and Fluid Flow. Hemisphere Publishing Corporation, Washington, USA.
Shrestha, K., Anderson, W., Kuehl, J., 2018. Langmuir turbulence in coastal zones: structure and length scales. J. Phys. Oceanogr. 48, 1089–1115.
Shrestha, K., Anderson, W., Tejada-Martínez, A.E., Kuehl, J., 2019. Orientation of coastal-zone Langmuir cells forced by wind, wave, and mean current at variable obliquity. J. Fluid Mech. 879, 716–743.
Shrestha, K., Anderson, W., 2020. Coastal Langmuir circulations induce phase-locked modulation of bathymetric stress. Environ. Fluid Mech. 20, 873–884.
Sinha, N., Tejada-Martínez, A.E., Akan, C., Grosch, C.E., 2015. Toward a K-profile parameterization of Langmuir turbulence in shallow coastal shelves. J. Phys. Oceanogr. 45, 2869–2895.
Skyllingstad, E.D., Denbo, D.W., 1995. An ocean large-eddy simulation of Langmuir circulations and convection in the surface mixed layer. J. Geophys. Res. 100 (C5), 8501–8522.
Smyth, W., Skyllingstad, E., Crawford, G., Wijesekera, H., 2002. Nonlocal fluxes and Stokes drift effects in the K-profile parameterization. Ocean Dynam. 52, 104–115.
Stommel, H., 1949. Trajectories of small bodies sinking slowly through convection cell. J. Mar. Res. 8, 24–29.
Tejada-Martínez, A.E., Grosch, C.E., Gargett, A.E., Polton, J.A., Smith, J.A., MacKinnon, J.A., 2009. A hybrid spectral/finite-difference large-eddy simulator of turbulent processes in the upper ocean. Ocean Model. 30, 115–142.
Tejada-Martínez, A.E., Grosch, C.E., 2007. Langmuir turbulence in shallow water: Part II. Large-eddy simulation. J. Fluid Mech. 576, 63–108.
Thorpe, S.A., 2004. Langmuir circulation. Annu. Rev. Fluid Mech. 36, 55–79.
Wilcox, D., 1994. Turbulence Modeling for CFD, second ed. DCW Industries, Inc., La Cañada, CA, USA.